iScience

Article

Blue light impairs cornea and corneal wound healing by downregulating VCAM1 partly

How does blue light pollution impair cornea and delay corneal epithelial wound healing?

Kuangqi Chen, Le Jin, Yingying Wen, ..., Chen Xie, Jianping Tong, Ye Shen

xiechenzju@163.com (C.X.)
idrtong@zju.edu.cn (J.T.)
idrshen@zju.edu.cn (Y.S.)

Highlights

Blue light impairs cornea and delays corneal epithelial wound healing

Blue light downregulates VCAM1 in corneal epithelial cells *in vivo* and *in vitro*

Blue light inhibits VCAM1 to promote apoptosis and ROS in corneal epithelial cells

Blue light inhibits VCAM1 to decrease AKT and migration in corneal epithelial cells
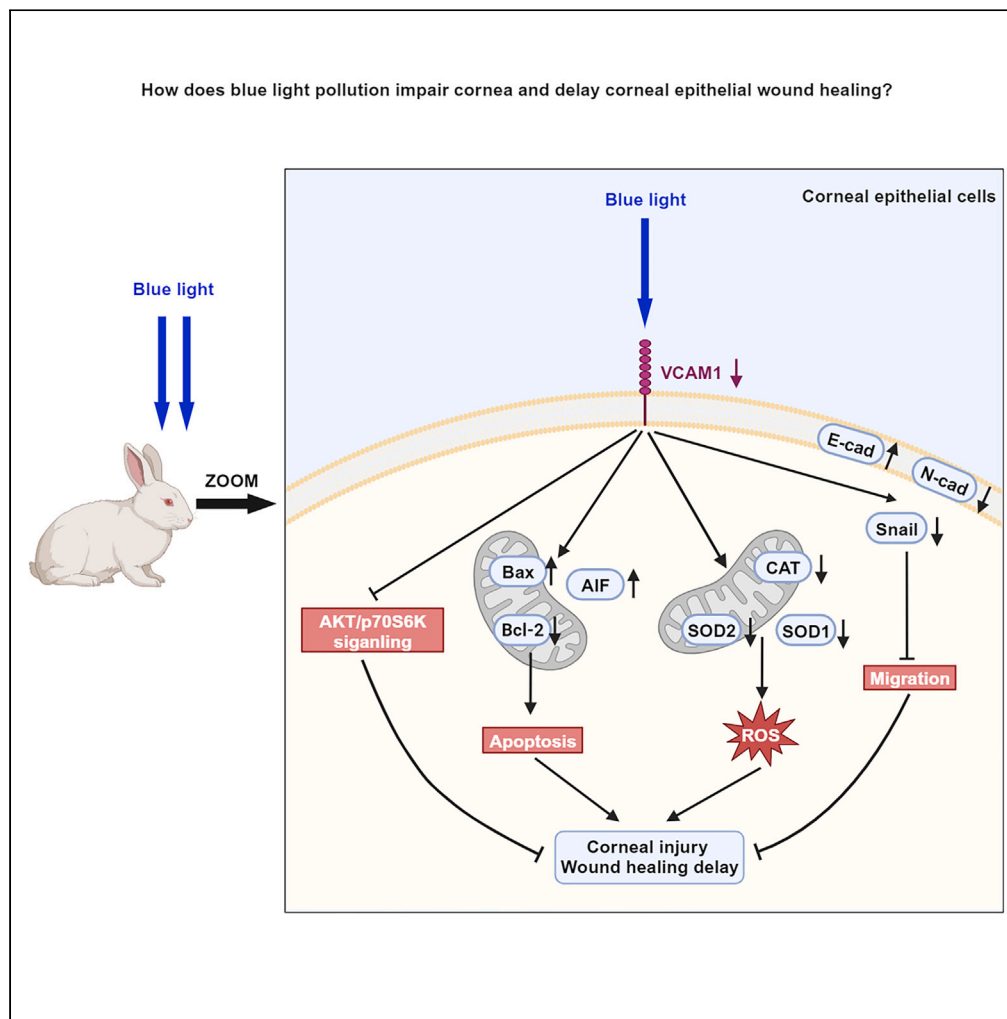
Article

Blue light impairs cornea and corneal wound healing by downregulating VCAM1 partly

Kuangqi Chen,[1,2] Le Jin,[1,2] Yingying Wen,[1,2] Qianjie Yang,[1] Xiang Li,[1] Liyue Zhang,[1] Liyin Wang,[1] Yutong Xia,[1] Zhitong Chen,[1] Chen Xie,[1,*] Jianping Tong,[1,*] and Ye Shen[1,3,*]

SUMMARY

This study aimed to investigate the effects of long-term pollution from different wavelengths of light on the corneal epithelium (CE) and identify potential biomarkers. Rabbits were exposed to red, green, blue, white, and environmental light for 6 weeks. The CE was assessed using various techniques such as fluorescein sodium staining, transcriptome sequencing, electron microscopy, and molecular assays. In human corneal epithelial cells (hCECs), the downregulation of vascular cell adhesion molecule 1 (VCAM1) in response to blue light (BL) pollution was observed. This downregulation of VCAM1 inhibited migration, increased reactive oxygen species (ROS) levels, and apoptosis, and inhibited the AKT/p70 S6 kinase cascade in hCECs. Animal experiments confirmed that BL pollution caused similar effects on the rabbit cornea, including increased ROS production, apoptosis, delayed wound healing, and decreased VCAM1 expression. Overall, BL-induced VCAM1 downregulation may impair CE and wound healing and promote ROS and apoptosis *in vitro* and *in vivo*.

INTRODUCTION

With the wide use of light-emitting diodes, eye tissue damage caused by artificial light pollution (especially by light-emitting diodes, LEDs) has received increasing attention from ophthalmologists and scientific researchers. The light that makes up an LED source includes red light (wavelength ranging from 620 to 760 nm, RL), green light (500–560 nm, GL) and blue light (400–480 nm, BL). BL is visible light, second only to ultraviolet light in wavelength, and has a greater ability to penetrate body tissue than ultraviolet light.[1] Moreover, the harmful effects of BL on the retina have been extensively studied. BL induces excessive reactive oxygen species (ROS) production, which damages photoreceptor cells and retinal pigment epithelium cells.[2] *In vitro* studies revealed that BL had the same phototoxicity to corneal and conjunctival epithelial cells. BL within a specific spectrum can induce ROS production and cell death, and a hypertonic environment can enhance the phototoxicity of BL.[3,4] Moreover, Lee et al. used LED monochromatic light at wavelengths of 630 nm, 525 nm, and 410 nm to irradiate mice with an energy dose of 50 J/cm^{2} and found that the tear film rupture time of mice polluted by BL was significantly reduced and was accompanied by a significant increase in inflammatory factors and ROS.[5]

Located at the outmost part of the eyeball, the cornea acts as both a mechanical and immune barrier of the eyes, and it can converge light from the external environment. Structurally, the cornea is composed of the corneal epithelium (CE), Bowman layer, corneal stroma, Descemet layer, and corneal endothelium from the outside to the inside. The CE consists of five to seven layers of laminated flattened epithelial cells, known as corneal epithelial cells (CECs), and is situated at the outermost layer of the cornea. Functionally, the CE acts as an immune and mechanical barrier in the eye, converges light, and maintains the homeostasis of the ocular surface microenvironment. As one of the most metabolically active structural cells in corneal tissue, CECs have several special functions, including proliferation, self-renewal, migration, adhesion, intercellular connectivity, and barrier functions. Clinically, corneal epithelial injury and delayed wound healing of the CE may be caused by trauma, pathogen infection, chemical injury, radiation, excessive light pollution, and other factors. Indeed, CEC dysfunction is closely related to corneal epithelial injury.

Vascular cell adhesion molecule 1 (VCAM1) has been shown to be a widely distributed adhesion protein on the membranes of vascular cells, epithelial cells, and tumor cells. Functionally, VCAM1 plays a role in inhibiting intercellular adhesion and promoting cell migration, proliferation, epithelial mesenchymal transformation, and metastasis in tumor cells by regulating cellular signal transduction.[6,7] Specifically, VCAM1 can bind with the integrin α4/β1 complex on the plasma membrane to regulate diverse downstream signaling cascades, such as the extracellular-signal-regulated kinase 1/2 signaling pathway and phosphatidylinositol 3-kinase (PI3K)/AKT signaling pathway.[6]

Recently, excessive and inappropriate light pollution caused by the wide use of artificial light sources has damaged CE, and its pathogenic mechanism has attracted increasing attention. Although many studies have shown that BL pollution causes corneal epithelial injury, there
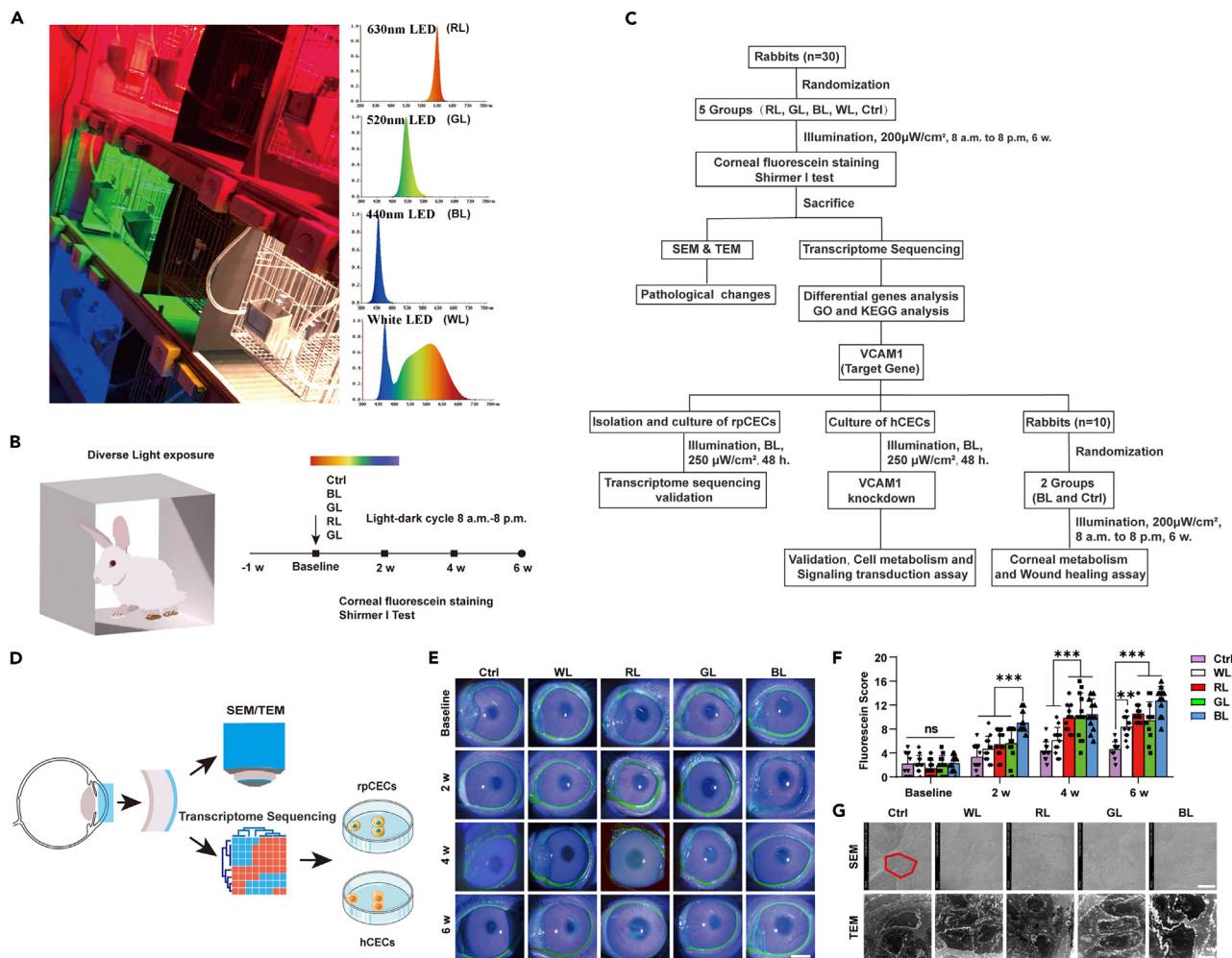
Figure 1. Experimental design and BL- and WL-pollution-induced corneal epithelial injury in rabbits

(A) Rabbit cages and spectra of the LED lights. Single-wavelength LED light sources (RL, red light; GL, green light; BL, blue light) were selected for the experiment with an irradiance of 0.2 mW/cm^2, and 500 lx illumination was selected for white light (WL).

(B) The rabbits were kept in a standard rabbit cage (50 cm × 42 cm × 35 cm). The LED panel was placed on the top of the cage. Cages with different lights were separated by black partitions to minimize interference. The illumination system automatically set the daily light-dark cycle at 12 h, and the rabbits were illuminated continuously for 6 weeks.

(C) A comprehensive flow diagram showing the objectives of the different experiments and their mutual connection to the conclusion commensurate with the primary aim of this study.

(D) The corneal epithelial parameters of rabbits were extracted, and transcriptome sequencing and verification were conducted.

(E) A typical photograph showing a sodium-fluorescein-dyed eye surface.

(F) Rabbit corneal fluorescein sodium staining scores before and after pollution to different LED light sources (n = 6).

(G) SEM and TEM images of the rabbit corneal epithelium after irradiation with different LED light sources. ns, not significant; *p < 0.05, **p < 0.01, ***p < 0.001. The data are shown as the mean ± SD. Statistical analysis was performed with two-way ANOVA followed by multiple comparisons. See also Figure S1.

have been no relevant studies on the effect of VCAM1 on the functions of hCECs in response to pollution with different light sources, especially BL. We aimed to determine the regulatory roles of VCAM1 in hCECs and the rabbit cornea in response to light pollution, which may provide a potential target for treating light-pollution-associated corneal epithelial injury and delayed wound healing.

RESULTS

BL pollution causes corneal injury to rabbit corneas

The main wavelengths and spectra are listed in Figure 1A, and the main experimental processes are listed in Figures 1B–1D. For the animal experiments, we used sodium fluorescein dye staining, and after 2 weeks of light pollution, the corneas in the BL group showed a few spots. Over the next 4 weeks, the number of spots gradually increased more than that in the control (Ctrl) group (Figure 1E). After

Figure 2. Rabbit corneal transcriptomics analysis revealed that the adhesion-associated protein VCAM1 was significantly decreased by BL pollution

(A) Differentially expressed genes in the blue light (BL), control (Ctrl), red light (RL), and green light (GL) groups.

(B) Pearson correlation analysis of the samples.

(C) Heatmap showing differentially expressed genes in the BL, Ctrl, RL, and GL groups (n = 3). The red rectangle indicates the location of VCAM1.

(D) Volcano map showing differentially expressed genes in the BL group and the Ctrl group. The red rectangles indicate VCAM1.

(E) GO enrichment bar plot of differentially expressed genes in the BL group and Ctrl group. The red rectangle indicates the VCAM1-associated cellular component.

(F) GO enrichment scatterplot of differentially expressed genes in the BL group and Ctrl group. The red rectangle indicates VCAM1-associated cellular metabolism.

(G) KEGG enrichment bar plot showing differentially expressed genes in the BL group and Ctrl group. The red rectangle indicates VCAM1-associated cellular processes and environmental information processing.

(H) KEGG enrichment scatterplot of differentially expressed genes in the BL group and Ctrl group. The red rectangle indicates VCAM1-associated cellular metabolism. See also Figure S1.

2 weeks of light pollution, the fluorescein score in the BL group was significantly higher than that in the Ctrl group and other experimental groups. However, at 4 and 6 weeks, there was no significant difference between the scores in the RL and GL groups and that in the BL group (Figure 1F). Moreover, scanning electron microscopy (SEM) showed that after BL pollution, the hexagonal structure of the rabbit CE was blurred, and the point-like microvilli structure on the surface was reduced (Figure 1G). Transmitting electron microscopy (TEM) showed that the distance between CECs was increased in the BL group, and the cell junctions were loose (Figure 1G). However, after 4 and 6 weeks of pollution with light, there was no significant difference in tear secretion among the five groups, indicating that there was no association between tear secretion and corneal injury caused by BL pollution (Figure S1A). Overall, we concluded that BL pollution caused injury in rabbits.

VCAM1 is significantly decreased by BL pollution *in vivo* and *in vitro*

Transcriptome sequencing revealed that compared with those in the control group, 166 genes were upregulated and 143 genes were downregulated (Figure 2A). Subsequently, differential gene heatmaps and volcano maps showed that, compared with that in the control group, VCAM1 was significantly decreased in the BL group but was not significantly changed in the RL and GL groups (Figures 2B and 2C). In addition, GO enrichment analysis showed that most of the differentially expressed genes between the BL group and the control group were located in the cytoplasm, integral components of the membrane, and plasma membrane, and these differentially expressed genes may regulate cell chemotaxis and cell adhesion in rabbit corneas (Figures 2D and 2E). Similarly, Kyoto Encyclopedia of Genes and Genomes (KEGG) enrichment analysis indicated that cellular community—eukaryotes, signaling molecules and interactions, and signal transduction were associated with differentially expressed genes (Figure 2F). Furthermore, the KEGG enrichment scatterplot revealed that cell adhesion molecules (CAMs) were enriched (Figure 2G). These metabolic processes have been demonstrated to be VCAM1-related processes. In addition, we analyzed the molecular interaction network of differentially expressed genes in the rabbit corneal transcriptome by STRING, which revealed that VCAM1 may directly interact with C-C motif chemokine 19 (CCL19), ATP-binding cassette sub-family G member 1 (ABCG1), and tyrosine-protein kinase Kit (KIT) and indirectly interact with lipoprotein lipase (LPL), nuclear receptor subfamily 1 group H member 3 (NR1H3), AKT2, β-actin (ACTB), and transgelin (TAGLN) (Figure S1B). Taken together, transcriptome sequencing indicated that VCAM1 expression in rabbit corneas was only significantly decreased after 6 weeks of BL pollution.

Subsequently, we further verified the accuracy of the transcriptome sequencing data. Cell culture, RNA extraction, and reverse transcription were performed on rabbit primary CECs (rpCECs). Afterward, several genes with significant changes in the transcriptome sequencing data were randomly selected for verification. The quantitative reverse transcription polymerase (RT-qPCR) chain reaction results proved that tripartite motif-containing 25 (TRIM25), metalloproteinase inhibitor 4 (TIMP4), cyclin B1 (CCNB1), Caspase 10 (Cas-10), nuclear receptor subfamily 1 group D member 1 (NR1D), lengsin (LGSN), and apolipoprotein D (APOD) were significantly changed in rpCECs after 48 h of BL pollution (Figure 3A). As expected, in hCECs, the mRNA expression of keratin 8 (KRT8), netrin1 (NTN1), mitogen-activated protein kinase (MAPK12), protein-arginine deiminase type-3 (PADI3), selenium-binding protein (SELENBP), and Caspase 10 (Cas-10) was significantly changed after 48 h of BL pollution (Figure 3B). More importantly, we further detected the expression of VCAM1 by RT-qPCR and western blot (WB) analysis in the Ctrl and BL groups, and the results revealed that VCAM1 mRNA and protein expression was significantly inhibited by 6 weeks of BL pollution (Figures 3C–3E). Similarly, we revealed that in rpCECs and hCECs, 48 h of BL pollution significantly decreased the mRNA expression levels of VCAM1 (Figure 3F).

To further study the role of VCAM1 in hCECs, we used RNA interference techniques to knock down VCAM1 at the mRNA level *in vitro*. As expected, the mRNA expression of VCAM1 was significantly decreased in the si-VCAM1 group compared with the si-negative control (si-NC) group (Figure 3F). Similarly, the protein expression of VCAM1 was significantly decreased in the si-VCAM1, BL + si-NC, and BL + si-VCAM1 groups compared with the si-NC group (Figures 3G and 3H). In addition, we further verified the efficiency of VCAM1 overexpression by plasmid transfection of hCECs. The cell experiments indicated that the mRNA and protein expression of VCAM1 after 48 h of BL pollution was effectively increased and was significantly higher than that in the BL + overexpression Vector (BL + OE Vector) group and higher than that in the OE-Vector group (Figures S1C–S1E). Collectively, these results indicated that VCAM1 knockdown and 48 h of BL pollution significantly reduced VCAM1 expression levels *in vivo* and *in vitro*.
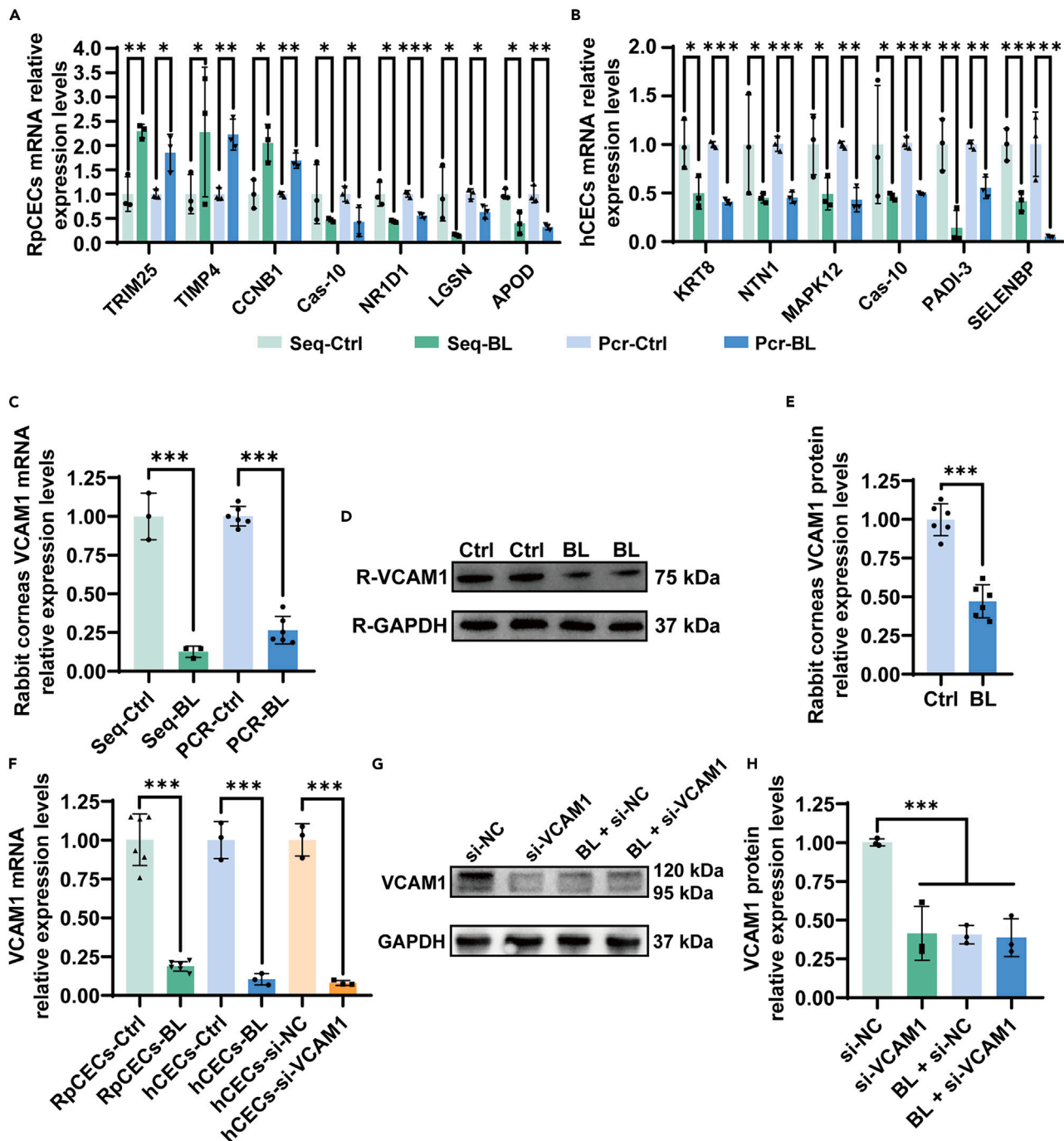
Figure 3. Transcriptome sequencing data validation and VCAM1 knockdown efficiency

(A) Validation of transcriptome sequencing of rabbit primary CECs (rpCECs) via RT-qPCR (n = 3).

(B) Validation of transcriptome sequencing of hCECs via RT-qPCR (n = 3).

(C) VCAM1 mRNA expression in rabbit corneas was determined by transcriptome sequencing (n = 3) and RT-qPCR (n = 6).

(D and E) VCAM1 protein expression in rabbit corneas was determined by WB analysis (n = 6).

(F) Validation of VCAM1 mRNA knockdown efficiency in rpCECs and hCECs and the downregulation of VCAM1 mRNA expression after 48 h of BL pollution in hCECs (n = 6 for rpCECs, n = 3 for hCECs).

(G and H) WB analysis of VCAM1 after 48 h of BL pollution and/or VCAM1 RNA interferon (n = 3). ns, not significant; *p < 0.05, **p < 0.01, ***p < 0.001. The data are shown as the mean ± SD. Statistical analysis was performed with unpaired Student's t test and/or one-way ANOVA followed by multiple comparisons. See also Figure S1.
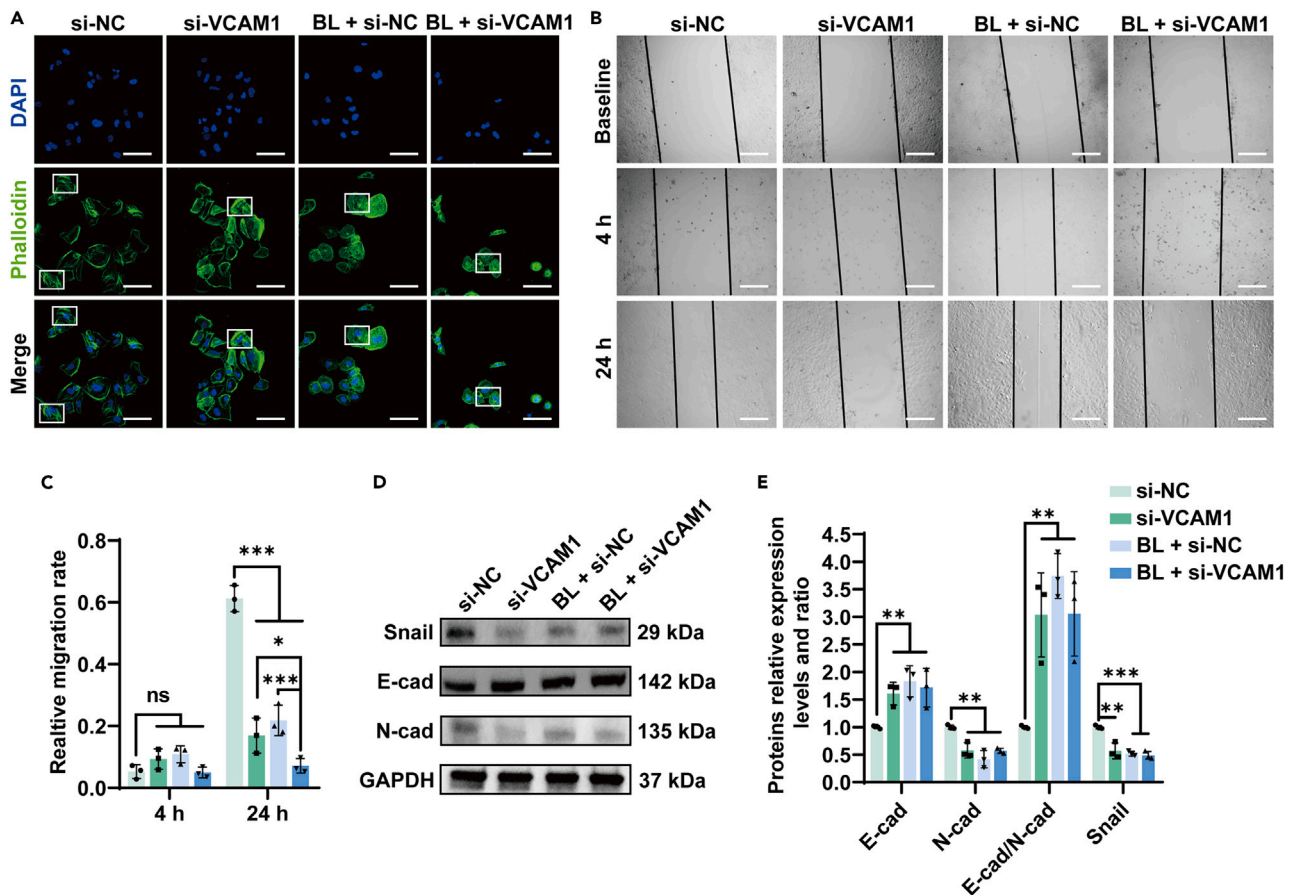
Figure 4. VCAM1 downregulation induced by BL pollution inhibits the migration of hCECs *in vitro*

(A) The cytoskeleton was stained with phalloidin, and the nucleus was stained with DAPI after 48 h of BL pollution and/or VCAM1 knockdown. Scale bar: 40 μm.

(B) The migration rate of hCECs after 48 h of BL pollution and/or VCAM1 knockdown was determined by a cell scratch assay. Scale bar: 100 μm.

(C) Statistical analysis of the hCEC migration rate, as determined by cell scratch experiments (n = 3).

(D and E) WB and semiquantitative analysis of Snail, E-cad, and N-cad and the ratio of E-cad/N-cad after 48 h of BL pollution and/or VCAM1 knockdown (n = 3). ns, not significant; *p < 0.05, **p < 0.01, ***p < 0.001. The data are shown as the mean ± SD. Statistical analysis was performed with one-way and two-way ANOVA tests, followed by multiple comparisons. See also Figure S2.

The downregulation of VCAM1 induced by BL pollution inhibits the migration of hCECs

We used 4′,6-diamidino-2-phenylindole (DAPI) and phalloidin to label the nucleus and F-actin in hCECs, respectively (Figure 4A). The results showed a decrease in microfilaments in all three groups compared with that in the si-NC group. In addition, cell scratch experiments showed that VCAM1 knockdown and 48 h of BL pollution significantly reduced hCEC migration compared with that in the si-NC group, and the combination of these two treatments further inhibited hCEC migration (Figures 4B and 4C). Subsequently, WB experiments further showed that 48 h of BL pollution, VCAM1 knockdown, and the combination of these two treatments significantly reduced Snail and N-cadherin (N-cad) expression and increased E-cadherin (E-cad) protein expression (Figures 4D and 4E). Moreover, cell rescue experiments showed that in response to BL pollution, VCAM1 overexpression reversed the increase in E-cad protein expression and the decrease in N-cad protein expression caused by 48 h of BL pollution, and the E-cad/N-cad ratio was decreased to the normal level. More interestingly, the protein expression of Snail was completely restored by VCAM1 overexpression and was significantly higher than that in the OE-Vector group (Figures S2A and S2B). Overall, we can conclude that the downregulation of VCAM1 in response to BL pollution inhibits the migration of hCECs *in vitro*.

The downregulation of VCAM1 induced by BL pollution promotes ROS and apoptosis and inhibits cell viability and AKT/p70 S6 kinase (p70S6K) signaling *in vitro*

To further study the effect of VCAM1 downregulation on apoptosis and ROS levels in hCECs after 48 h of BL pollution, we examined apoptosis levels and changes in ROS levels under VCAM1 downregulation and/or 48 h of BL pollution. Specifically, JC-1 staining indicated that the ratio of JC-1 aggregates/monomers was significantly decreased by 48 h of BL pollution and/or VCAM1 knockdown, which revealed that the mitochondrial membrane potential was significantly decreased (Figures 5A and 5E). Moreover, the 2′,7′-dichlorodihydrofluorescein diacetate
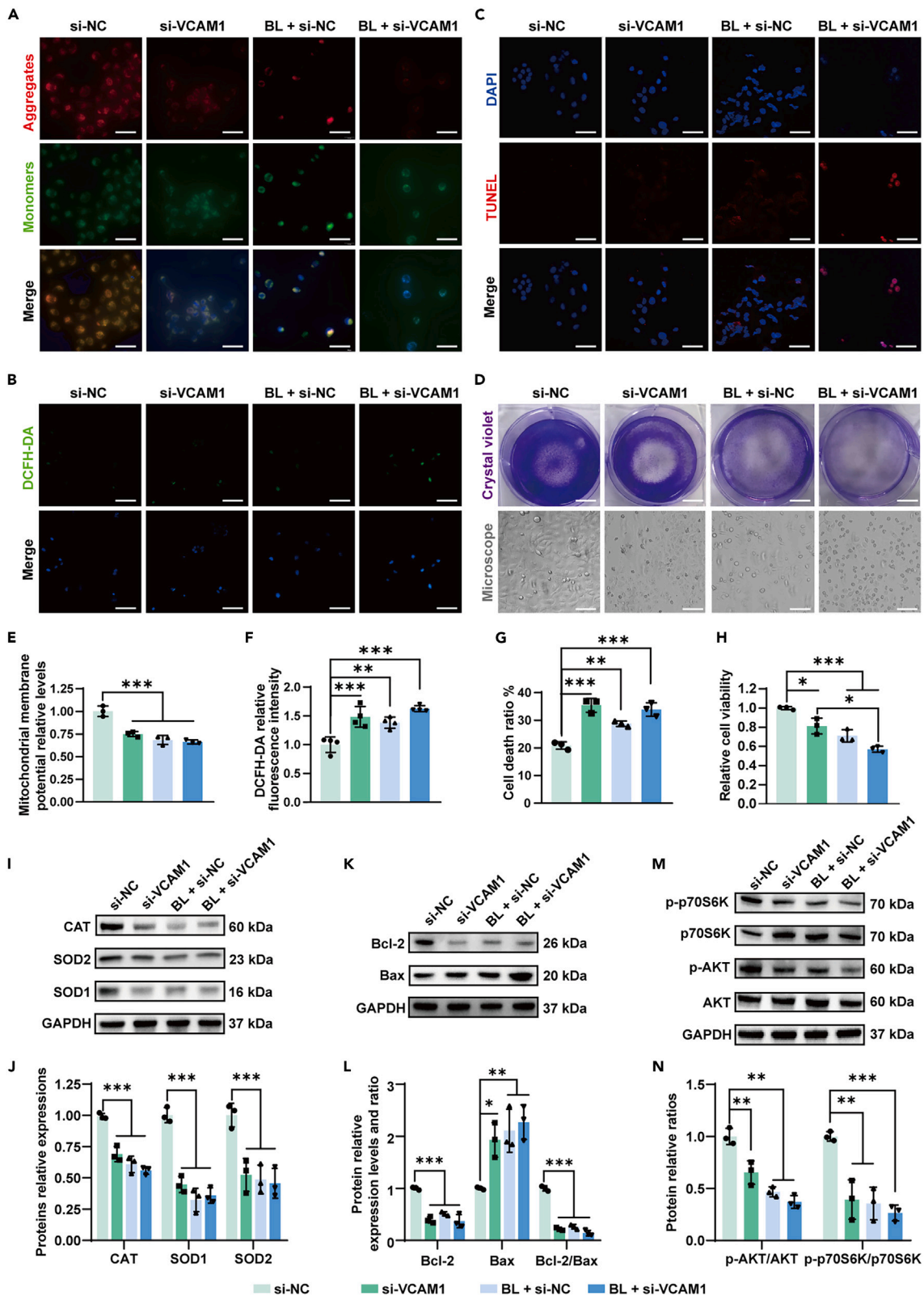
Figure 5. VCAM1 downregulation induced by BL pollution promotes ROS production and apoptosis and inhibits viability and the AKT/p70S6K cascade in hCECs *in vitro*

(A) JC-1 staining assay of mitochondrial membrane potential in hCECs under 48 h of BL pollution and/or VCAM1 knockdown. Scale bar: 20 μm.

(B) DCFH-DA staining of hCECs after 48 h of BL pollution and/or VCAM1 knockdown. Scale bar: 40 μm.

(C) TUNEL staining of hCECs after 48 h of BL pollution and/or VCAM1 knockdown. Scale bar: 20 μm.

(D) Crystal violet staining and microscopic observation of hCECs after 48 h of BL pollution and/or VCAM1 knockdown. Scale bars: 1 cm and 40 μm.

(E) Semiquantitative analysis of ROS levels in hCECs by DCFH-DA staining (n = 4).

(F) Semiquantitative analysis of relative mitochondrial membrane potential by JC-1 staining of hCECs (n = 3).

(G) LDH assay and semiquantitative analysis of hCECs after 48 h of BL pollution and/or VCAM1 knockdown (n = 3).

(H) Relative viability of hCECs after 48 h of BL pollution and/or VCAM1 knockdown, as determined by CCK-8 assays (n = 3).

(I and J) WB and semiquantitative analysis of CAT, SOD1, and SOD2 after 48 h of BL pollution and/or VCAM1 knockdown (n = 3).

(K and L) WB and semiquantitative analysis of Bcl-2 and Bax and the relative ratio of Bcl-2/Bax after 48 h of BL pollution and/or VCAM1 knockdown (n = 3).

(M and N) WB and semiquantitative analysis of p-p70S6K, p70S6K, p-AKT, and AKT and relative ratios of p-p70S6K/p70S6K and p-AKT/AKT in hCECs after 48 h of BL pollution and/or VCAM1 knockdown (n = 3). ns, not significant; *$p < 0.05$, **$p < 0.01$, ***$p < 0.001$. The data are shown as the mean $\pm$ SD. Statistical analysis was performed with one-way ANOVA followed by multiple comparisons. See also Figure S2.

(DCFH-DA) staining assay indicated that VCAM1 knockdown and 48 h of BL pollution significantly increased ROS levels in hCECs compared with those in the si-NC group (Figures 5B and 5F). In addition, WB analysis demonstrated that catalase (CAT), superoxide dismutase 1 (SOD1), and SOD2 levels were significantly decreased by VCAM1 knockdown and/or 48 h of BL pollution (Figures 5I and 5J). In addition, cell rescue experiments showed that after 48 h of BL pollution, VCAM1 overexpression restored CAT, SOD1, and SOD2 at the protein level.

Subsequently, L-lactate dehydrogenase (LDH) assays showed that VCAM1 knockdown and 48 h of BL pollution significantly increased the cell death ratio in hCECs. Although BL pollution alone could aggravate cell death, the extent of damage caused by BL pollution was lower than that caused by VCAM1 knockdown (Figure 5G). Similarly, the cell counting kit-8 (CCK-8) assay revealed that VCAM1 knockdown and 48 h of BL pollution significantly decreased cell viability compared with that in the si-NC group, and the combination of these two treatments further impaired cell viability (Figure 5H).

The terminal deoxynucleotidyl transferase dUTP nick end labeling (TUNEL) assay showed that the apoptosis levels in the si-VCAM1, BL + si-NC, and BL + si-VCAM1 groups were increased compared with those in the si-NC group (Figure 5C). In addition, crystal violet staining and microscopic observations revealed that VCAM1 knockdown and/or 48 h of BL pollution delayed cell proliferation, reduced cell density, and increased the proportion of apoptotic hCECs (Figure 5D). The WB results further revealed that 48 h of BL pollution, VCAM1 knockdown, and the combination of these two treatments significantly reduced B-cell lymphoma-2 (Bcl-2) and increased BCL2-associated X (Bax) protein expression (Figures 5K and 5L). In addition, the ratio of Bcl-2/Bax was dramatically decreased by 48 h of BL pollution and/or VCAM1 knockdown (Figure 5L). Furthermore, cell rescue experiments showed that in response to BL pollution, VCAM1 overexpression restored the increase in Bax and the decrease in Bcl-2 at the protein level, and the Bcl-2/Bax ratio was decreased to the normal level (Figures S2E and S2F).

Collectively, these results indicated that VCAM1 downregulation by BL pollution promotes ROS production and apoptosis and inhibits cell viability and the AKT/p70S6K signaling cascade in hCECs *in vitro*.

Long-term BL pollution inhibits corneal epithelial wound healing and migration and induces ROS production and apoptosis in rabbit corneas

We further investigated the effects of long-term blue light pollution on ROS production, apoptosis levels, the AKT/p70S6K signaling pathway, and wound healing in CE in rabbits.

First, we detected the ROS production rate in the rabbit cornea in the absence or presence of 6 weeks of BL pollution. Specifically, dihydroethidium (DHE) staining showed that more ROS production was observed in the BL group than in the Ctrl group (Figure 6A). More importantly, immunohistochemistry (IHC) and WB analysis of rabbit corneas showed that the protein expression of SOD1 was significantly decreased by 6 weeks of BL pollution (Figures 6D, 6E, 6H, and 6I). Moreover, the RT-qPCR results revealed a significant decrease in SOD1, SOD2, and CAT levels in rabbit corneas (Figure 6G). These results demonstrated that long-term BL pollution could lead to a significant increase in ROS production in rabbit corneas.

In rabbits in the Ctrl and BL groups, TUNEL staining revealed that after 6 weeks of BL pollution, an increase in DNA damage was observed in the CE in the BL group (Figure 6B). The RT-qPCR assay also revealed a significant increase in Bax and a significant decline in Bcl-2 in rabbit corneas (Figure 6G). Moreover, WB and IHC analysis of rabbit corneas showed that the protein expression of Bax was significantly increased by 6 weeks of BL pollution (Figures 6D, 6F, 6H, and 6I). These results demonstrated that long-term BL pollution could increase apoptosis in rabbit corneas.

Subsequently, we detected the corneal epithelial wound healing rate of rabbits in the Ctrl and BL groups, and the results showed that 6 weeks of BL pollution significantly delayed wound healing in the rabbit CE (Figures 6C and 6E). And the RT-qPCR results revealed a significant increase in E-cad and a significant decline in N-cad and Snail in rabbit corneas (Figure 6G). More importantly, IHC and WB analysis of rabbit corneas showed that the protein expression of N-cad was significantly decreased by 6 weeks of BL pollution (Figures 6D, 6F, 6H, and 6I). These results demonstrated that long-term BL pollution could lead to a significant delay in corneal epithelial wound healing and cell migration in rabbit corneas.
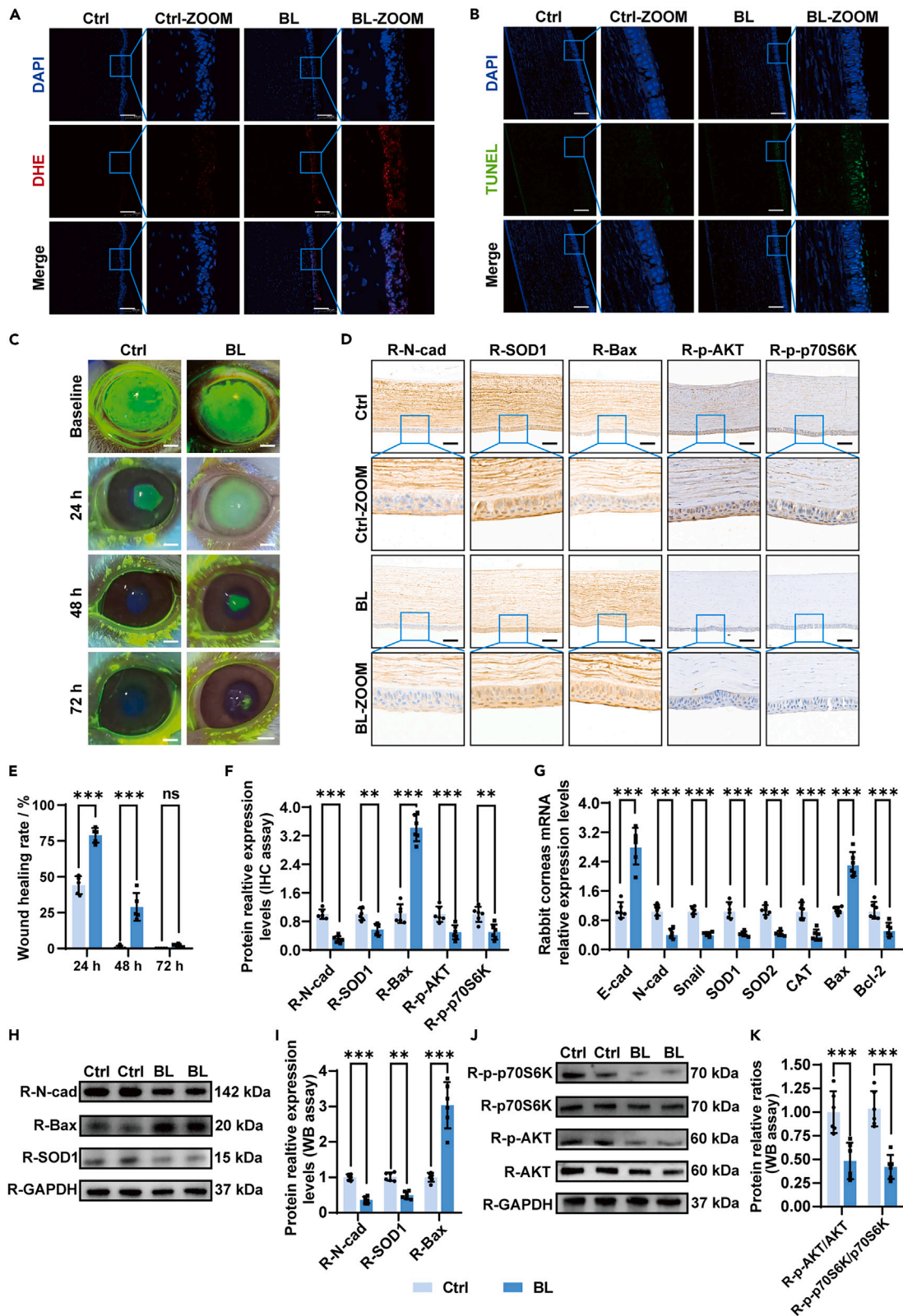
Figure 6. Long-term BL pollution induces CEC apoptosis and ROS production and inhibits corneal epithelial wound healing and CEC migration in rabbits

(A) DHE staining of rabbit corneas after 6 weeks of BL pollution. Scale bar: 200 μm.

(B) TUNEL staining of rabbit corneas after 6 weeks of BL pollution. Scale bar: 200 μm.

(C and E) Rabbit corneal epithelial wound healing assay and semiquantitative analysis after 6 weeks of BL pollution (n = 5). Scale bar: 5 mm.

(D and F) Rabbit corneal IHC staining and semiquantitative analysis of SOD1, N-cad, Bax, p-AKT, and p-70S6K after 6 weeks of BL pollution (n = 5). Scale bar: 200 μm.

(G) Rabbit corneal RT-qPCR and semiquantitative analysis after 6 weeks of BL pollution (n = 6).

(H and I) Rabbit corneal WB and semiquantitative analysis of SOD1, N-cad, and Bax after 6 weeks of BL pollution (n = 6).

(J and K) Rabbit corneal WB and semiquantitative analysis of ratios of p-AKT/AKT and p-p70S6K/p70S6K after 6 weeks of BL pollution (n = 6). ns, not significant; *p < 0.05, **p < 0.01, ***p < 0.001. The data are shown as the mean ± SD. Statistical analysis was performed with an unpaired Student's t test. See also Figure S2.

In addition, IHC assays revealed that both phosphorylated AKT (p-AKT) and phosphorylated p70S6K (p-p70S6K) were significantly downregulated by 6 weeks of BL pollution (Figures 6D and 6F). WB assays also showed that the ratios of p-AKT/AKT and p-p70S6K/p70S6K were significantly decreased by 6 weeks of BL pollution (Figures 6J and 6K). These results demonstrated that the AKT/p70S6K cascade was inactivated by BL pollution.

Overall, we can conclude that long-term BL pollution inhibits corneal epithelial wound healing and the AKT/p70S6K cascade and induces apoptosis and ROS production in rabbit corneas.

DISCUSSION

BL pollution is one of the most important pathogenic mechanisms of CE damage caused by LED screens. With the development and popularization of narrow-wavelength LED technology, we can further study CE damage caused by different wavelengths of light that make up the LED light source. In our study, we found that BL pollution caused corneal epithelial injury, a delay in corneal epithelial wound healing, AKT/p70S6K inactivation, apoptosis increase, and excessive ROS production in rabbit corneas. The expression levels of VCAM1 were significantly downregulated in rabbit corneas and hCECs exposed to BL. Furthermore, BL-induced VCAM1 downregulation may inhibit cell viability and promote apoptosis and ROS production in hCECs. Moreover, these effects may be associated with the inactivation of the VCAM1/AKT/p70S6K signaling cascade in hCECs. In addition, VCAM1 overexpression in hCECs can restore these cellular impairments.

Eye damage and metabolic changes caused by light pollution have been widely reported. For instance, BL pollution significantly inhibited cell viability and autophagy and induced cell death, apoptosis, inflammation, mitochondrial dysfunction, and ROS in the retina *in vitro* and *in vivo*.[8-11] In addition, BL pollution can decrease cellular viability and promote inflammation and ROS production in hCECs.[4] However, red light has been shown to protect CE. Specifically, in hCECs, red light pollution has a positive effect on cell survival, migration, proliferation, and differentiation *in vitro*.[12] In our study, we revealed that BL pollution could increase apoptosis and ROS production and reduce viability and migration in hCECs. Furthermore, BL and white light pollution caused corneal injury, delays in corneal epithelial wound healing and migration, apoptosis, and ROS production in rabbit corneas. In addition, it has been shown that RL and GL pollution did not cause significant damage to rabbit corneas.

VCAM1, which is also named CD106, was first identified in 1989 as an endothelial adhesion receptor involved in leukocyte recruitment in cellular immune responses. VCAM1 has been extensively studied in a variety of disease models, including Parkinson disease, heart failure, ischemic stroke, and multiple cancers.[13-17] Specifically, VCAM1 helps regulate inflammation-related vascular adhesion and the cross-endothelial migration of white blood cells, and it is thought to be an oncogene for different cancer types.[18] Structurally, human VCAM1 contains an extracellular domain with 6 or 7 immunoglobulin-like domains, a transmembrane domain, and a cytoplasmic domain.[19] Mechanistically, VCAM1 binds to integrin α4β1 to activate multiple intracellular signal transduction pathways, such as the JAK/STAT1 signaling pathway in gastric cancer and MAPK signaling.[18] However, in recent years, there have been few studies on VCAM1 in the cornea.[20] Hakami et al. realized that inhibiting NAPDH oxidase 4 significantly reduced the increase in VCAM1 in response to alkali burn injury to the mouse cornea, relieving oxidative stress and fibrosis of the cornea.[20] In this study, we revealed for the first time that VCAM1 was significantly decreased in rabbit corneas, rpCECs, and hCECs in response to BL pollution. More importantly, VCAM1 downregulation by BL pollution *in vitro* could induce cell death and apoptosis and inhibit ROS, migration, and cell viability. VCAM1 overexpression in hCECs could restore these cellular impairments.

There is no consensus on the relationship between VCAM1 and AKT.[21,22] Most studies have indicated that integrin α4β1 is involved in the phosphorylation of AKT by VCAM1.[6] Moreover, Chen et al. found that VCAM-1 aggregation upregulated ezrin phosphorylation, which directly induced PI3K and AKT phosphorylation and then activated cell survival and apoptosis signaling in breast and lung cancer cells.[23] However, PI3K/AKT signaling was also shown to be an upstream regulatory signaling cascade of VCAM1.[22] Specifically, the expression and secretion of VCAM1 can be increased via the IL1β/IL1R/PI3K/AKT/NADPH oxidase/ROS/NF-κB cascade in glioblastoma, which plays a key role in the regulation of tumor-associated monocyte/macrophage polarization and osteoblast differentiation.[21,22,24] Mechanistically, the PI3K/AKT/mTOR/p70S6K signaling pathway has been proven to be a crucial regulatory pathway in a variety of cells, including CECs.[25-29] Specifically, the PI3K/AKT/p70S6K signaling pathway, which is activated by phosphorylation, significantly promotes cell proliferation, differentiation, migration, autophagy, and survival and inhibits apoptosis and oxidative stress in CECs and wound healing in the CE.[30-32] Moreover, p70S6K has been associated with cell apoptosis and oxidative stress in various tissues.[33-35] Our study showed that VCAM1 downregulation caused by RNA interference or BL pollution could significantly decrease activation of the AKT/p70S6K cascade. More importantly, VCAM1 overexpression in hCECs could restore the inactivation of the AKT/p70S6K cascade. Thus, BL-pollution-induced

VCAM1 downregulation caused AKT/p70S6K inactivation, which may be an important reason for the increase in apoptosis and oxidative stress, as well as the inhibition of hCEC migration.

Overall, we can conclude that long-term BL pollution caused corneal epithelial injury, delays in rabbit corneal epithelial wound healing and migration, apoptosis, and ROS production, and a decrease in VCAM1 expression *in vivo*. BL-pollution-induced VCAM1 downregulation can inhibit cell migration and viability, promote ROS and apoptosis, and inactivate the AKT/p70S6K cascade in hCECs. These results may provide a potential target for treating BL-pollution-induced corneal epithelial injury.

Limitations of study

We must acknowledge that our study had several limitations. First, due to the limitations of tissue engineering techniques and the particularity of corneal structure, *in vivo* conditional knockdown or overexpression of VCAM1 in rabbit CE is difficult to achieve. This could provide indirect assistance in constructing a knockout or overexpression model of VCAM1 in rabbit CE. In addition, although the regulatory effect of VCAM1 on AKT has been widely verified, we cannot rule out that there may be other regulatory mechanisms by which VCAM1 affects the metabolism of hCECs. Moreover, corneal tissue samples were used for transcriptome sequencing, but only hCECs and rpCECs were used for cell experiments. Therefore, we cannot rule out the impact of the transcriptome expression profiles of corneal endothelial and stromal cells on the experiment. Indeed, VCAM1 is widely expressed in endothelial cells; thus, the mechanism by which VCAM1 affects corneal endothelial injury caused by BL pollution needs further investigation.

STAR★METHODS

Detailed methods are provided in the online version of this paper and include the following:

- KEY RESOURCES TABLE
- RESOURCE AVAILABILITY
  - Lead contact
  - Materials availability
  - Data and code availability
- EXPERIMENTAL MODEL AND STUDY PARTICIPANT DETAILS
  - Animals
  - Cell culture
- METHOD DETAILS
  - LED light pollution
  - Fluorescein sodium staining
  - SEM
  - TEM
  - Transcriptome sequencing and analysis
  - Total RNA extraction and qRT-PCR
  - WB analysis
  - RNA interference and VCAM1 overexpression
  - IHC
  - Cell scratch and corneal wound healing assay
  - Crystal violet staining
  - TUNEL apoptosis detection
  - ROS assay
  - Cytoskeleton fluorescence staining
  - Cell viability assay
  - LDH cytotoxicity assay
- QUANTIFICATION AND STATISTICAL ANALYSIS

SUPPLEMENTAL INFORMATION

Supplemental information can be found online at https://doi.org/10.1016/j.isci.2023.108448.

REFERENCES

1. Krutmann, J., and Berneburg, M. (2021). [Sun-damaged skin (photoaging): what is new? Hautarzt 72, 2–5.

2. Jaadane, I., Boulenguez, P., Chahory, S., Carré, S., Savoldelli, M., Jonet, L., Behar-Cohen, F., Martinsons, C., and Torriglia, A. (2015). Retinal damage induced by commercial light emitting diodes (LEDs). Free Radic. Biol. Med. 84, 373–384.

3. Niwano, Y., Kanno, T., Iwasawa, A., Ayaki, M., and Tsubota, K. (2014). Blue light injures corneal epithelial cells in the mitotic phase in vitro. Br. J. Ophthalmol. 98, 990–992.

4. Marek, V., Mélik-Parsadaniantz, S., Villette, T., Montoya, F., Baudouin, C., Brignole-Baudouin, F., and Denoyer, A. (2018). Blue light phototoxicity toward human corneal and conjunctival epithelial cells in basal and hyperosmolar conditions. Free Radic. Biol. Med. 126, 27–40.

5. Lee, H.S., Cui, L., Li, Y., Choi, J.S., Choi, J.H., Li, Z., Kim, G.E., Choi, W., and Yoon, K.C. (2016). Influence of Light Emitting Diode-Derived Blue Light Overpollution on Mouse Ocular Surface. PLoS One 11, e0161041.

6. Zhou, Z., Zhou, Q., Wu, X., Xu, S., Hu, X., Tao, X., Li, B., Peng, J., Li, D., Shen, L., et al. (2020). VCAM-1 secreted from cancer-associated fibroblasts enhances the growth and invasion of lung cancer cells through AKT and MAPK signaling. Cancer Lett. 473, 62–73.

7. (2022). VCAM1 Mediates Innate Immune Tolerance of Hematopoietic and Leukemic Stem Cells. Cancer Discov. 12.

8. Zhu, S., Li, X., Dang, B., Wu, F., Gou, K., Wang, C., and Lin, C. (2022). Hydrogen sulfide protects retina from blue light-induced photodamage and degeneration via inhibiting ROS-mediated ER stress-CHOP apoptosis signal. Redox Rep. 27, 100–110.

9. Alaimo, A., Liñares, G.G., Bujjamer, J.M., Gorojod, R.M., Alcon, S.P., Martínez, J.H., Baldessari, A., Grecco, H.E., and Kotler, M.L. (2019). Toxicity of blue led light and A2E is associated to mitochondrial dynamics impairment in ARPE-19 cells: implications for age-related macular degeneration. Arch. Toxicol. 93, 1401–1415.

10. Feng, J., Chen, X., Sun, X., Wang, F., and Sun, X. (2014). Expression of endoplasmic reticulum stress markers GRP78 and CHOP induced by oxidative stress in blue light-mediated damage of A2E-containing retinal pigment epithelium cells. Ophthalmic Res. 52, 224–233.

11. Yang, P.M., Cheng, K.C., Huang, J.Y., Wang, S.Y., Lin, Y.N., Tseng, Y.T., Hsieh, C.W., and Wung, B.S. (2021). Sulforaphane inhibits blue light-induced inflammation and apoptosis by upregulating the SIRT1/PGC-1α/Nrf2 pathway and autophagy in retinal pigment epithelial cells. Toxicol. Appl. Pharmacol. 421, 115545.

12. Núñez-Álvarez, C., and Osborne, N.N. (2019). Enhancement of corneal epithelium cell survival, proliferation and migration by red light: Relevance to corneal wound healing. Exp. Eye Res. 180, 231–241.

13. Perner, C., Perner, F., Gaur, N., Zimmermann, S., Witte, O.W., Heidel, F.H., Grosskreutz, J., and Prell, T. (2019). Plasma VCAM1 levels correlate with disease severity in Parkinson's disease. J. Neuroinflammation 16, 94.

14. Maglinger, B., Sands, M., Frank, J.A., McLouth, C.J., Trout, A.L., Roberts, J.M., Grupke, S., Turchan-Cholewo, J., Stowe, A.M., Fraser, J.F., and Pennypacker, K.R. (2021). Intracranial VCAM1 at time of mechanical thrombectomy predicts ischemic stroke severity. J. Neuroinflammation 18, 109.

15. Pinho, S., Wei, Q., Maryanovich, M., Zhang, D., Balandrán, J.C., Pierce, H., Nakahara, F., Di Staulo, A., Bartholdy, B.A., Xu, J., et al. (2022). VCAM1 confers innate immune tolerance on haematopoietic and leukaemic stem cells. Nat. Cell Biol. 24, 290–298.

16. Franklin, R.A., Liao, W., Sarkar, A., Kim, M.V., Bivona, M.R., Liu, K., Pamer, E.G., and Li, M.O. (2014). The cellular and molecular origin of tumor-associated macrophages. Science 344, 921–925.

17. Zhang, S., Xie, B., Wang, L., Yang, H., Zhang, H., Chen, Y., Wang, F., Liu, C., and He, H. (2021). Macrophage-mediated vascular permeability via VLA4/VCAM1 pathway dictates ascites development in ovarian cancer. J. Clin. Invest. 131, e140315.

18. Shen, J., Zhai, J., You, Q., Zhang, G., He, M., Yao, X., and Shen, L. (2020). Cancer-associated fibroblasts-derived VCAM1 induced by H. pylori infection facilitates tumor invasion in gastric cancer. Oncogene 39, 2961–2974.

19. Schlesinger, M., and Bendas, G. (2015). Vascular cell adhesion molecule-1 (VCAM-1)–an increasing insight into its role in tumorigenicity and metastasis. Int. J. Cancer 136, 2504–2514.

20. Hakami, N.Y., Dusting, G.J., Chan, E.C., Shah, M.H., and Peshavariya, H.M. (2020). Wound Healing After Alkali Burn Injury of the Cornea Involves Nox4-Type NADPH Oxidase. Invest. Ophthalmol. Vis. Sci. 61, 20.

21. Jiang, Y., Zhang, L., and Tian, H. (2023). MicroRNA-149 improves osteoarthritis via repression of VCAM-1 and inactivation of PI3K/AKT pathway. Exp. Gerontol. 174, 112103.

22. Shen, C.K., Huang, B.R., Yeh, W.L., Chen, C.W., Liu, Y.S., Lai, S.W., Tseng, W.P., Lu, D.Y., and Tsai, C.F. (2021). Regulatory effects of IL-1β in the interaction of GBM and tumor-associated monocyte through VCAM-1 and ICAM-1. Eur. J. Pharmacol. 905, 174216.

23. Chen, Q., Zhang, X.H.F., and Massagué, J. (2011). Macrophage binding to receptor VCAM-1 transmits survival signals in breast cancer cells that invade the lungs. Cancer Cell 20, 538–549.

24. Hatori, A., Fujii, Y., Kawase-Koga, Y., Ogasawara, T., Chikira, J., Minami, S., Yamakawa, D., and Chikazu, D. (2023). VCAM-1 and GFPT-2: Predictive markers of osteoblast differentiation in human dental pulp stem cells. Bone 166, 116575.

25. Cao, Q., Li, Y., Li, Y., and Li, L. (2021). miR-151-5p alleviates corneal allograft rejection by activating PI3K/AKT signaling pathway and balancing Th17/Treg after corneal transplantation via targeting IL-2Rα. Ann. Transl. Med. 9, 1410.

26. Shang, Z., Li, C., Liu, X., Xu, M., Zhang, X., Li, X., Barnstable, C.J., Zhao, S., and Tombran-Tink, J. (2021). PEDF Gene Deletion Disrupts Corneal Innervation and Ocular Surface Function. Invest. Ophthalmol. Vis. Sci. 62, 18.

27. Liu, W., Lin, T., and Gong, L. (2023). ZD6474 Attenuates Fibrosis and Inhibits Neovascularization in Human Pterygium by Suppressing AKT-mTOR Signaling Pathway. J. Ocul. Pharmacol. Therapeut. 39, 128–138.

28. Wang, G., Long, J., Gao, Y., Zhang, W., Han, F., Xu, C., Sun, L., Yang, S.C., Lan, J., Hou, Z., et al. (2019). SETDB1-mediated methylation of Akt promotes its K63-linked ubiquitination and activation leading to tumorigenesis. Nat. Cell Biol. 21, 214–225.

29. Chen, M., Choi, S., Wen, T., Chen, C., Thapa, N., Lee, J.H., Cryns, V.L., and Anderson, R.A.

(2022). A p53-phosphoinositide signalosome regulates nuclear AKT activation. Nat. Cell Biol. *24*, 1099–1113.

30. Chen, K., Li, Y., Zhang, X., Ullah, R., Tong, J., and Shen, Y. (2022). The role of the PI3K/AKT signalling pathway in the corneal epithelium: recent updates. Cell Death Dis. *13*, 513.

31. Liu, Y., Di, G., Wang, Y., Chong, D., Cao, X., and Chen, P. (2021). Aquaporin 5 Facilitates Corneal Epithelial Wound Healing and Nerve Regeneration by Reactivating Akt Signaling Pathway. Am. J. Pathol. *191*, 1974–1985.

32. Li, S., Tang, L., Zhou, J., Anchouche, S., Li, D., Yang, Y., Liu, Z., Wu, J., Hu, J., Zhou, Y., et al. (2022). Sleep deprivation induces corneal epithelial progenitor cell over-expansion through disruption of redox homeostasis in the tear film. Stem Cell Rep. *17*, 1105–1119.

33. Guo, X., and Liang, M. (2022). Metformin alleviates dexamethasone-induced apoptosis by regulating autophagy via AMPK/mTOR/p70S6K in osteoblasts. Exp. Cell Res. *415*, 113120.

34. Hu, R., Dong, W., Liang, Q., Wang, F., Ou, M., Li, Z., Ren, Y., Wu, X., Liu, Y., and Wang, W. (2020). A Litopenaeus vannamei p70S6K gene is involved in the antioxidative and apoptosis under low temperature. Fish Shellfish Immunol. *106*, 656–665.

35. Yang, T., Xiao, Y., Liu, S., Luo, F., Tang, D., Yu, Y., and Xie, Y. (2023). Isorhamnetin induces cell cycle arrest and apoptosis by triggering DNA damage and regulating the AMPK/mTOR/p70S6K signaling pathway in doxorubicin-resistant breast cancer. Phytomedicine *114*, 154780.

36. Guo, X., Dang, W., Li, N., Wang, Y., Sun, D., Nian, H., and Wei, R. (2022). PPAR-α Agonist Fenofibrate Ameliorates Sjögren Syndrome-Like Dacryoadenitis by Modulating Th1/Th17 and Treg Cell Responses in NOD Mice. Invest. Ophthalmol. Vis. Sci. *63*, 12.

37. Pauly, A., Brignole-Baudouin, F., Labbé, A., Liang, H., Warnet, J.M., and Baudouin, C. (2007). New tools for the evaluation of toxic ocular surface changes in the rat. Invest. Ophthalmol. Vis. Sci. *48*, 5473–5483.

38. Wan, L., Bai, X., Zhou, Q., Chen, C., Wang, H., Liu, T., Xue, J., Wei, C., and Xie, L. (2022). The advanced glycation end-products (AGEs)/ROS/NLRP3 inflammasome axis contributes to delayed diabetic corneal wound healing and nerve regeneration. Int. J. Biol. Sci. *18*, 809–825.

STAR★METHODS

KEY RESOURCES TABLE

REAGENT or RESOURCE	SOURCE	IDENTIFIER
Antibodies		
Rabbit monoclonal anti-GAPDH	Cell Signaling Technology	CAT#5174S
Mouse monoclonal anti-GAPDH	Abclonal	CAT#AC002
Rabbit monoclonal anti-E-Cadherin	Cell Signaling Technology	CAT#3195S
Rabbit monoclonal anti-Bax	Cell Signaling Technology	CAT#41162
Rabbit polyclonal anti-Bax	Bioss	CAT#bs-0127R
Mouse monoclonal anti-Bcl-2	Cell Signaling Technology	CAT#15071S
Rabbit monoclonal anti-N-Cadherin	Cell Signaling Technology	CAT#13116
Mouse monoclonal anti-N-Cadherin	Invitrogen	CAT#MA1-2002
Rabbit monoclonal anti-VCAM1	Cell Signaling Technology	CAT#13662
Rabbit polyclonal anti-VCAM1	Bioss	CAT#bs-0920R
Rabbit polyclonal anti-p70 S6 Kinase	Cell Signaling Technology	CAT#9202
Rabbit monoclonal anti-Phospho-p70 S6 Kinase	Cell Signaling Technology	CAT#97596
Rabbit monoclonal anti-Akt	Cell Signaling Technology	CAT#4685S
Rabbit monoclonal anti-Phospho-Akt	Cell Signaling Technology	CAT#4060
Rabbit monoclonal anti-Phospho-Akt	Abclonal	CAT#AP1208
Rabbit monoclonal anti-Catalase	Cell Signaling Technology	CAT#12980
Rabbit polyclonal anti-Superoxide dismutase 1	Abcam	CAT#ab13498
Rabbit monoclonal anti-SOD2	Abcam	CAT#ab68155
Chemicals, peptides, and recombinant proteins		
Trizol	Invitrogen	CAT#15596026
Hoechst 33342 Staining Solution	Beyotime	CAT#C1027
Phalloidin- Alexa Fluor 488	Beyotime	CAT#C2201S
Critical commercial assays		
two-step RT-PCR Kit with SYBR Green	Vazyme	CAT#MQ101-02
Cell Counting Kit-8 (CCK-8)	Sigma-Aldrich	CAT#96992
LDH Cytotoxicity Assay Kit	Beyotime	CAT#C0017
DCFH-DA Assay Kit	Beyotime	CAT#S0033
DHE Assay Kit	Beyotime	CAT#S0063
TUNEL Apoptosis Assay Kit (for cell experiment)	Beyotime	CAT#C1089
TUNEL BrightGreen Apoptosis Detection Kit (for rabbit experiment)	Vazyme	CAT#A112
Deposited data		
RNA-Seq	lc-bio	Gene Expression Omnibus number: GSE242331
Experimental models: Cell lines		
Human corneal epithelial cells (hCECs)	Riken Cell Bank	N/A
Oligonucleotides		
siRNA of VCAM1 in *Homo Sapiens* sense: GGC-UGGAGAUAGACUUACUTT; antisense: –AGUAAGUCUAUCUCCAGCCTT.	Genepharma	N/A
-Primers for QRT-PCR, see Table S1	This paper	N/A

(Continued on next page)

Continued

REAGENT or RESOURCE	SOURCE	IDENTIFIER
Recombinant DNA		
pcDNA™3.1 Mammalian Expression Vector	Invitrogen	CAT# V79520
Software and algorithms		
Cutadapt(1.9)	Cutadapt	https://cutadapt.readthedocs.io/
hisat2(2.0.4)	Johns Hopkins University	https://daehwankimlab.github.io/hisat2/
StringTie	Johns Hopkins University	http://ccb.jhu.edu/software/stringtie/
gffcompare	Johns Hopkins University	N/A
SDS (v.1.4)	Johns Hopkins University	N/A
SPSS(22.0)	IBM	N/A
GraphPad Prism	GraphPad Prism	https://www.graphpad.com/scientificsoftware/prism/
Image J	National Institute of Health	https://ImageJ.nih.gov/ij/

RESOURCE AVAILABILITY

Lead contact

Further information and requests for resources and reagents should be directed to and will be fulfilled by the lead contact, Ye Shen (idrshen@zju.edu.cn).

Materials availability

The materials in this article will be shared by the lead contact upon reasonable request.

Data and code availability

- The RNA-seq data have been deposited in the Gene Expression Omnibus (GSE242331) and are publicly available as of the date of publication.
- This paper does not report original code.
- Any additional information required to reanalyze the data reported in this paper is available from the lead contact upon request.

EXPERIMENTAL MODEL AND STUDY PARTICIPANT DETAILS

Animals

All animal experiments were approved by the Animal Experiment Ethics Committee of the School of Medicine, Zhejiang University. In this study, the animals were divided into 5 groups (6 female rabbits in each group, 12 eyes, weight: 1.9 to 2.1 kg, 2 to 3-mouth-old at kittenhood). In addition to the four light groups, rabbits raised in a normal environment without special light were used as controls. Each rabbit was kept in a standard rabbit cage (size: 50 cm × 42 cm × 35 cm). Except for those in the Ctrl group, all rabbit cages were covered in the dark with a light curtain. In addition, cages with different lights were separated by black partitions to minimize interference. The LED panel was placed on the top of the cage. The rabbit's eyes were approximately 10 cm away from the light source. Single-wavelength LED light sources (RL, GL, BL, WL) with an irradiance of 0.2 mW/cm^2 were selected for the experiment. The illumination system automatically set the daily light-dark cycle for 12 h, and the rabbits were illuminated continuously for 6 w. In a standard environment, the corneal fluorescein staining score was evaluated every 2 w (fixed time: 2:00 p.m. to 4:00 p.m.). The rabbits were killed after 6 w of light and dark cycle illumination with an LED light source.

Cell culture

hCECs were purchased from Riken Cell Bank in Japan and cultured according to the instructions. hCECs were cultured in DMEM/F12 medium containing 10% fetal bovine serum (FBS) in a 37°C incubator containing 5% CO$_2$.

To extract rpCECs, the rabbits were euthanized by an overdose of pentobarbital sodium. Sterile ophthalmic scissors were used to cut along the corneal limbus to obtain a relatively intact cornea. The isolated cornea was washed three times with PBS and cut into small pieces with ophthalmic scissors. The cornea was placed in a petri dish with the outer side (convex) facing down and left for approximately 30 min to fully adhere to the wall. Next, 6 ml of Dulbecco's modified Eagle's medium (China) containing 20% FBS (Gibco, New Zealand) was added.

After 2-3 d, the corneal patches were removed with eye tweezers. At that time, the cells in the culture dish were mainly rpCECs. The rpCECs were passaged every 2 to 3 d. The rpCECs were suspended and added to six-well plates, with approximately 300,000 cells per well. After the cells had adhered, 48 h of BL pollution (440 nm, 200 $\mu W/cm^2$) with the same wavelength and intensity as the animal experiment was used.

METHOD DETAILS

LED light pollution

Part of the experimental light source used a phosphor-conversion (PC) LED light radiation illumination system designed and provided by China Hongyan Electric Technology Co., Ltd., which included monochromatic light of 630 nm (RL), 520 nm (GL) and 440 nm (BL) and WL with a color temperature of 4500 K. All spectral energy distributions were professionally tested by the company. The light intensity during the pollution period was measured and adjusted by a spectral colorimeter (Hopocolor OHSP-350, Hangzhou).

Fluorescein sodium staining

Sodium fluorescein test paper (Tianjin Jingming New Technology Development Co., Ltd.) was soaked in normal saline, the lower eyelid of the rabbit was gently opened, sodium fluorescein was applied to the conjunctival sac, and the eyes were closed several times to evenly coat them with the dye. A digital slit lamp analysis system (Chongqing Kanghua Ruiming Technology Co., Ltd.) was switched to a cobalt blue filter, the fluorescence staining of the cornea was observed, and the photos were recorded and scored. The grading process was performed by the same person. The cornea was divided into four quadrants, and each quadrant was divided into 0~4 points according to the staining degree and staining area. Finally, the total score was determined as follows (0~16 points): 0: no corneal fluorescence staining; 1: scattered dot staining, < 30; 2: slightly dense dot staining, > 30, but not diffuse; 3: severe diffuse staining, but no flaky staining; and 4: fusion and sheet staining.[36,37]

SEM

The cornea was fixed in 2.5% glutaraldehyde at 4°C overnight and then washed in phosphate buffer (PBS, pH 7.4) 3 times. The sample was fixed with 1% osmic acid solution for 1 to 2 h. The samples were dehydrated by a series of gradient concentrations of ethanol (30%, 50%, 70%, 80%, 90% and 95%). Then, the sample was treated with 100% ethanol and new 100% ethanol. After being dehydrated, the sample was dried in a Hitachi HCP-2 critical point dryer. After being coated, the treated sample was observed with a Hitachi SU-8010 scanning electron microscope.

TEM

For TEM, the samples were subjected to double fixation and dehydrated with gradient concentrations of ethanol (30%, 50%, 70%, and 80%). Then, the samples were transferred to 90% and 95% acetone solutions. Finally, the samples were treated twice with pure acetone. Then, gradient infiltration was performed, and the samples were successively treated with Spurr embedding agent, acetone and a mixture of Spurr embedding agent plus acetone. Finally, the samples were treated with pure embedding agent overnight. The next day, the samples were embedded after infiltration treatment and heated at 70°C overnight to obtain the embedded sample. The samples were sliced with a LEICA EM UC7 ultrathin microtome. The slices were dyed with lead citrate solution and 50% ethanol in a saturated solution of uranyl acetate for 5 to 10 min. Finally, they were observed by a Hitachi H-7650 transmission electron microscope.

Transcriptome sequencing and analysis

Total RNA was isolated from the sample and purified using TRIzol reagent (Invitrogen, USA) according to the manufacturer's protocol. Briefly, RNA quantity, purity, and integrity were assessed using a NanoDrop ND-1000, Bioanalyzer 2100, and agarose electrophoresis. A concentration > 50 ng/μL, RIN value > 7.0, OD260/280>1.8, and total RNA>1 μg met the requirements of downstream experiments. Oligo magnetic beads (Dynabeads Oligo, No. 25-61005, Thermo Fisher, USA) were used to specifically capture PolyA (polyadenylic acid)-bearing mRNA through two rounds of purification. The captured mRNA was fragmented at a high temperature by using a magnesium ion disruption kit (Nebnext magnesium RNA fragmentation module, article number E6150S, USA) for 5-7 min at 94°C. The fragmented RNA was subjected to reverse transcription (Invitrogen superscript II reverse transcriptase, No. 1896649) to synthesize cDNA. Then, *E. coli* DNA polymerase I (NEB, article number m0209) and RNase H (NEB, article number m0297) were used for double-stranded synthesis, and the compound double-stranded DNA and RNA were converted into double-stranded DNA. Then, dUTP Solution (Thermo Fisher, article number R0133) was added to the double-stranded DNA, and the ends of the double-stranded DNA were padded to be flat-stranded. Then, an A base was added to each end of the DNA so that it could be connected with a linker with a T base at the end, and the size of the fragment was screened and purified by magnetic beads. UDG enzyme (NEB, No. m0280) was used to digest the two strands and then predenatured by PCR at 95°C for 3 min, denatured at 98°C for 8 cycles of 15 s each, annealed at 60°C for 15 s, extended at 72°C for 30 s, and finally extended at 72°C for 5 min to form a library with a fragment size of 300 $\pm$ 50 bp. The library was then sequenced using an Illumina NovaSeq 6000 (PE150 mode). Off-board raw data in fastq format were processed using Cutadapt software (cutadapt-1.9) for interface removal. Clean data were obtained by removing low-quality and repeated sequences. The clean data were then compared to the genome using hisat2 (hisat2-2.0.4) and preliminarily assembled with StringTie (stringtie-1.3.4d. Linux_x86_64). Final assembly annotation was achieved by comparing transcripts

with reference annotation using gffcompare (gffcompare-0.9.8. Linux x86_64). Differential gene analysis was performed using edger in the R package, and fold change > 2 or < 0.5 (p < 0.05) indicated differentially expressed genes. GO and KEGG enrichment analyses were conducted. String (https://cn.string-db.org/), the Protein−Protein Interaction Networks and Functional Enrichment Analysis website were used to analyze the transcriptome sequencing results.

Total RNA extraction and qRT-PCR

The rabbits were euthanized by injecting an excess of pentobarbital sodium. Fresh corneal tissue samples were mixed with TRIzol reagent, broken and centrifuged to release the RNA, which was precipitated, washed to remove contaminants, dissolved, and tested for quality and concentration. For rpCECs and hCECs, after experimental intervention, the medium was removed. After adding TRIzol, the medium was aspirated, the cells were centrifuged to release the RNA, and the pollutants were removed by precipitation and washing. The RNA was dissolved, and the quality and concentration were determined by a Nanodrop 2000 (2000c, Thermo, USA).

qRT-PCR was performed using the two-step RT−PCR kit with SYBR Green (Vazyme, China) on a Thermal Cycler Dice TP800 Sequence Detection System (Takara, Shiga, Japan) according to the manufacturer's instructions. The cycle threshold (Ct) values were calculated using SDS v. 1.4 software. The mRNA levels of genes were calculated by the $2-\Delta\Delta Ct$ method. GAPDH was used as the internal control. The sequences of the primer pairs are shown in Table S1.

WB analysis

After experimental intervention, the plate was washed twice with PBS buffer for 10 min each. We added 200 μL of RIPA buffer to the six-well plate and then used a cell scraper to scrape the cells off the ice and lyse them for 30 min. The protein concentration was quantified by the BCA method, and then loading buffer (25% of the total volume) was added, mixed and incubated at 100°C for 5 min. For WB analysis, the soluble part of the total protein was separated by SDS−PAGE and transferred to nitrification fiber or PVDF membranes. Horseradish peroxidase (HRP)-conjugated specific antibodies were used for western blotting. The primary antibodies were as follow: anti-GAPDH (1:5000, 5174S, CST for hCECs; and 1:10000, AC002, ABclonal for rabbit corneas), anti-E-cad (1:1000, 3195S, CST), anti-Bax (1:1000, 41162, CST), anti-Bcl-2 (1:1000, 15071S, CST), anti-N-cad (1:1000, 13116, CST for hCECs; and 1:1000, MA12002, Thermo Fisher Scientific for rabbit corneas), anti-VCAM1 (1:1000, 13662, CST for hCECs, and 1:1000, bs-920r, Bioss for rabbit corneas), anti- p70S6K (1:1000, 9202, CST), anti-phospho-p70 S6 Kinase (p-p70S6K, 1:1000, 97596, CST), anti-p-AKT (1:1000, 4660, CST for hCECs; and 1:1000, AP1208, ABclonal for rabbit corneas), anti-AKT (1:1000, 4685, CST), anti-CAT (1:1000, 12980, CST), anti- SOD1 (1:2000, ab13498, Abcam), and anti-SOD2 (ab68155, Abcam).

RNA interference and VCAM1 overexpression

We designed a small interfering RNA (siRNA) targeting human VCAM1, and the sequences were as follows: sense: GGCUGGAGAUA GACUUACUTT; antisense: AGUAAGUCUAUCUCCAGCCTT. To overexpress human VCAM1, the VCAM1 cDNA fragment was inserted into the pcDNA3.1 vector (Invitrogen, USA), resulting in pcDNA3.1-VCAM1. We also used the following negative control siRNA (NC) in the cell experiments: sense: UUCUCCGAACGUGUCACGUTT, antisense: ACGUGACACGUUCGGAGAATT. Subsequently, transfection was performed according to the Jet prime kit instructions. Briefly, hCECs were cultured in 6-well or 24-well plates to approximately 50% confluence, and the medium was replaced with reduced serum medium (Opti-MEM, Gibco, New Zealand). The Jet prime transfection reagent and appropriate buffer were mixed proportionally and incubated at room temperature for 10 s. The transfection reagent was then mixed with the siRNA solution or pcDNA3.1 vector solution at the given ratio and incubated at room temperature for 10 min to form the transfection complex. The transfection complex was then slowly added to the medium containing the target cells, ensuring uniform coverage of the entire cell layer, and incubated at 37°C for 6 to 8 h, after which the cell treatments were performed.

IHC

The presence of N-cad, SOD1, Bax, p-AKT, and p70S6K in the Crtl and BL groups was assessed by IHC. To perform the staining, 4 μm sections were prepared, and the slides were initially dewaxed. Endogenous peroxidase activity was inhibited by using a peroxidase inhibitor (H_2O_2). The sections were incubated with primary antibodies, including anti-Bax (1:200, bs-0127r, Bioss), anti-N-cad (1:200, MA12002, Thermo Fisher Scientific), anti-SOD1 (1:200, ab13498, Abcam), anti- p-AKT (1:200, AP1208, ABclonal), and anti- p-p70S6K (1:100, 97596, CST) overnight at 4°C. Afterward, the sections were treated with a secondary antibody labeled with HRP for 1 h at 37°C. To visualize the staining, a solution of 3,3′-diaminobenzidine was added, which led to the development of a brown color. The stained sections were captured under a microscope (Nikon, Japan). ImageJ was used to quantify the pathological results.

Cell scratch and corneal wound healing assay

hCECs were inoculated into six-well plates at a seeding amount of 200,000 cells per well. Once the cells adhered to the plate walls and reached a fusion of 70%-80%, the medium was changed to reduced serum medium. Subsequently, we initiated treatment for BL pollution and siRNA transfection. After incubating at 37°C with 5% CO2 for 24 h, the serum-depleted medium was replaced with 10% serum medium. The hCECs were then incubated for an additional 24 h under either BL pollution or dark conditions to establish intact cell monolayers. Thereafter, a scratch was created using a pipette tip, and any debris and floating cells were removed by washing with PBS. The cells were then

incubated with serum-free medium at 37°C to allow migration and wound healing. Images of the scratch were captured at 0, 24 h, and 48 h after scratch creation. Then, the migration distance was analyzed using ImageJ software to quantify the cell migration rates.

Rabbits were intravenously anesthetized with pentobarbital sodium for eye immobilization. Standardized wounds of the corneas were created using Algerbrush II corneal rust ring remover (Alger Co., Lago Vista, TX). The wounds were stained with sodium fluorescein and observed at 0, 24, 48, and 72 h.[38] Photographic documentation of the cornea was performed after irradiation with 365 nm ultraviolet light. The wound closure rate and healing progress were analyzed using ImageJ software.

Crystal violet staining

The culture medium was removed, and the cells were carefully washed with PBS in six-well plates. A volume of 0.1 ml of a 10% methanol solution was added to each well to fix the cells for 30 s. The methanol solution was absorbed, 0.1 ml of crystal violet dye solution was added to each well, and the plate was left for 20 min at room temperature. The dye solution was gently shaken off, each well was washed twice with PBS, and the culture plate was placed upside down on absorbent paper to absorb moisture. A mobile phone camera was used to capture the images.

TUNEL apoptosis detection

To detect apoptosis, *in situ* TUNEL staining was performed on hCECs and rabbit corneas. hCECs were grown on 24-well plates, fixed with paraformaldehyde for 15 min and permeabilized with 0.1% Triton X-100 for 10 min. The plate was washed twice with PBS buffer for 10 min each. The TUNEL reaction mixture, which contained TdT enzyme and fluorescently labeled dUTP, was added (C1089, Beyotime, China) and incubated at 37°C for 30 min in the dark. The plate was washed twice with PBS buffer for 10 min each. Nuclei were stained with DAPI for 5 min at 37°C (C0002, Beyotime, China), and images were collected in the 594 nm channel with fluorescence microscopy (FV3000, Olympus, Japan).

Rabbit corneas were fixed with 4% paraformaldehyde, embedded in paraffin and sectioned to a thickness of 5 μm. TUNEL staining was performed using a commercially available kit (A112, Vazyme, China), and the sections were treated with a terminal deoxynucleotidyl transferase enzyme and nucleotide mixture. The plate was washed twice with PBS buffer for 10 min each. Nuclei were stained with DAPI for 5 min at 37°C (C0002, Beyotime, China), and images were collected in the 488 nm channel with a fluorescence microscope.

ROS assay

ROS levels were measured using a DCFH-DA kit (S0033S, Beyotime, China). DCFH-DA is a nonfluorescent membrane permeable compound that becomes fluorescent and membrane impervious upon oxidation. hCECs were seeded in 24-well plates and cultured at 37°C in 5% CO_2. After intervention, the DMEM was completely removed, and the cells were washed twice with PBS buffer for 10 min each. The cells were incubated with 20 μg/mL DCFH-DA at 37°C for 30 min in the dark. The plate was washed twice with PBS buffer for 10 min each. Nuclei were stained with Hoechst dye for 5 min at 37°C (C1026, Beyotime, China), and images were collected in the 488 nm channel with a fluorescence microscope.

Fresh rabbit corneas were sliced with OCT compound and then incubated with a 20 μg/mL DHE solution to allow penetration into the cells at 37°C for 30 min. DHE is a fluorescent probe that binds irreversibly to DNA (S0063, Beyotime, China). DHE is reduced by electrochemical reduction to a fluoro-hydroxyethidium (2-HE). Within the cell, 2-HE binds to the bases of nucleic acids (especially DNA) and emits a red fluorescent signal. The strength of this fluorescent signal is proportional to the level of ROS produced within the cell. The plate was washed twice with PBS buffer for 10 min each. Nuclei were stained with Hoechst dye for 5 min at 37°C, and images were collected in the 594 nm channel with a fluorescence microscope. The intensity of 2-HE fluorescence serves as an indicator of oxidative stress in the cornea.

Cytoskeleton fluorescence staining

hCECs were seeded in 24-well plates and cultured at 37°C in 5% CO_2. To label F-actin, after the indicated treatments, the DMEM was completely removed, and the cells were washed twice with PBS buffer for 10 min each. The cells were incubated with 10 μg/mL Alexa Fluor 488 phalloidin (C2201S, Beyotime, China) at 37°C for 30 min. The plate was washed twice with PBS buffer for 10 min each. Nuclei were stained with Hoechst dye for 5 min at 37°C, and images were collected in the 488 nm channel with a fluorescence microscope.

Cell viability assay

The viability of hCECs was analyzed using the CCK-8 assay (Sigma–Aldrich, USA). hCECs were inoculated on 96-well plates (Sarstedt, Germany) with 100 μL culture solution per well. After incubation, 10 μL of CCK-8 reagent was added to each well and incubated at 37°C in 5% CO_2 and 95% humidity for 3 h. The optical density was measured by a Bio-Tek ELx808 spectrophotometer (BioTek Instruments, USA) at a wavelength of 450 nm. The background signal was subtracted from all samples.

LDH cytotoxicity assay

According to the manufacturer's protocol, the Agappe LDH Kit was used to detect LDH release in the supernatant (Beyotime, C0017, China). After the indicated treatments, the culture media was collected and centrifuged to remove any remaining cell debris. The supernatant was then mixed with a reaction buffer containing the substrate for LDH. The reaction produces a colorimetric proportional to the amount of LDH

released. A spectrophotometer (Beckman Coulter DU-730, CA, USA) was used to measure a 3 min decline in the absorbance of LDH at 340 nm over time.

QUANTIFICATION AND STATISTICAL ANALYSIS

All data were statistically analyzed using SPSS 22.0 and GraphPad software 8.0. All experiments were replicated at least three times, and two groups were compared by unpaired t tests, while one-way or two-way ANOVA followed by Tukey multiple comparisons was performed for more than two groups. $P < 0.05$ was considered significant (* $p<0.05$; ** $p< 0.01$; *** $p< 0.001$). The data are shown as the mean $\pm$ SD. Moreover, we used ImageJ for image analysis and Adobe Illustrator 2023 for image arrangement and composition.